



Synthesis and novel properties of Q-silicon

Jagdish Narayan, Siba Sundar Sahoo, Naveen Joshi & Roger Narayan

To cite this article: Jagdish Narayan, Siba Sundar Sahoo, Naveen Joshi & Roger Narayan (2023) Synthesis and novel properties of Q-silicon, Materials Research Letters, 11:8, 688-696, DOI: [10.1080/21663831.2023.2224396](https://doi.org/10.1080/21663831.2023.2224396)

To link to this article: <https://doi.org/10.1080/21663831.2023.2224396>



© 2023 The Author(s). Published by Informa UK Limited, trading as Taylor & Francis Group.



[View supplementary material](#)



Published online: 21 Jun 2023.



[Submit your article to this journal](#)



Article views: 3861



[View related articles](#)



[View Crossmark data](#)



Citing articles: 5 [View citing articles](#)

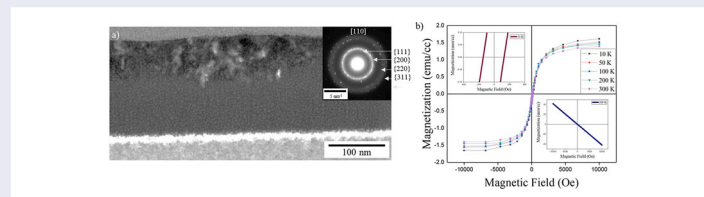
Synthesis and novel properties of Q-silicon

Jagdish Narayan, Siba Sundar Sahoo, Naveen Joshi and Roger Narayan

Department of Materials Science and Engineering, North Carolina State University, Raleigh, USA

ABSTRACT

We report the discovery of Q-silicon with an atomic density of 60% higher than crystalline silicon while keeping the bonding characteristics the same as normal silicon. Distinct amorphous phases are created, when one, two, or three tetrahedra are randomly packed, and a crystalline phase of Q-silicon is formed when subunit cells are arranged along $<110>$ directions with alternate holes. Nanosecond laser melting of amorphous silicon in an undercooled state and quenching have created Q-silicon with robust ferromagnetism compared to the diamagnetism of silicon. The blocking temperature of Q-silicon is estimated to be over 400 K, thus opening a new frontier for spin-based computing and atomic-level storage.



IMPACT STATEMENT

The discovery of Q-silicon having robust RT ferromagnetism will open a new frontier in atomic-scale spin-based devices and functional integration with nanoelectronics. Other properties of interest include enhanced hardness and superconductivity.

ARTICLE HISTORY

Received 11 April 2023

KEYWORDS

Q-silicon synthesis; RT ferromagnetism; nanosecond laser melting and quenching

Introduction

The pursuit of ferromagnetism in materials outside of transition metals and rare earths has excited scientists worldwide for a long time. This is because spin-polarized electrons can be used to process and store information with atomic resolution. However, materials with an even number of electrons such as carbon and silicon without unpaired spins were not considered seriously in terms of bulk ferromagnetism. The dangling bonds in bulk carbon and silicon materials usually reconstruct and eliminate sources of unpaired electrons. However, at the free surfaces of covalently bonded materials, steps and kinks can provide sources of dangling bonds and unpaired spins, which can lead to paramagnetism and ferromagnetism, provided these spins can achieve long-range ordering [1]. Our recent discovery showed the occurrence of robust ferromagnetism in Q-carbon, which consisted of randomly packed diamond tetrahedra. The bonding within the tetrahedra in Q-carbon was determined to be sp³ with

no dangling bonds. However, the bonding between the tetrahedra was a mixture of sp³ and sp² with an overall fraction of about 85% sp³ and 15% sp². Thus, dangling bonds and unpaired spins between the tetrahedra played a critical role in producing robust ferromagnetism in Q-carbon [2–5]. It should be mentioned that defect-induced intrinsic ferromagnetism has been observed in oxides and nitrides and other related materials with laser annealing, vacuum thermal annealing, and ion implantation [6,7]. In oxides, such as ZnO, ferromagnetism is related to paramagnetic Zn vacancies, which are coupled through oxygen vacancies for room-temperature ferromagnetism [6].

Here, we report, for the first time, the formation of Q-silicon after nanosecond laser melting of amorphous silicon layers and quenching from the undercooled state. The amorphous silicon produced by ion implantation showed a diamagnetic behavior, which turned ferromagnetic upon laser annealing. It is interesting to note that as-implanted amorphous silicon and Q-silicon

CONTACT Jagdish Narayan  narayan@ncsu.edu  Department of Materials Science and Engineering, North Carolina State University, Raleigh, 27695-7907, USA

 Supplemental data for this article can be accessed here. <https://doi.org/10.1080/21663831.2023.2224396>

© 2023 The Author(s). Published by Informa UK Limited, trading as Taylor & Francis Group. This is an Open Access article distributed under the terms of the Creative Commons Attribution-NonCommercial License (<http://creativecommons.org/licenses/by-nc/4.0/>), which permits unrestricted non-commercial use, distribution, and reproduction in any medium, provided the original work is properly cited. The terms on which this article has been published allow the posting of the Accepted Manuscript in a repository by the author(s) or with their consent.

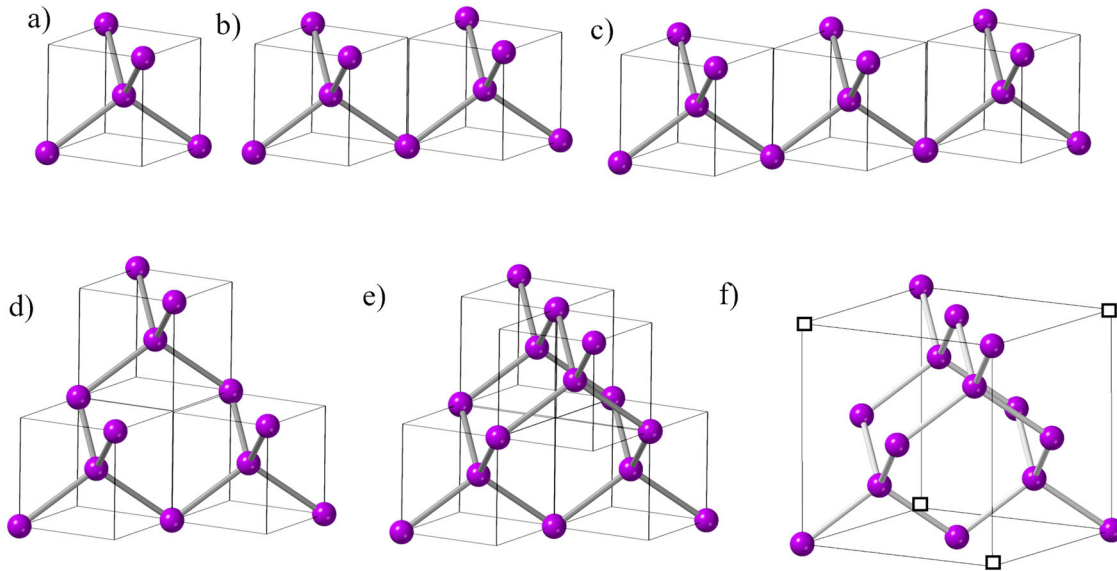


Figure 1. (a) Diamond tetrahedron D1 with central atom contained in $(a/2, a/2, a/2)$ cube; (b) Two D1 tetrahedra connected along $<110>$ direction; (c) Three D1 tetrahedra along $<110>$ direction; (d) Three D1 tetrahedra: two in $<110>$ direction (first layer) and one $<1-10>$ direction (second layer); (e) Four D1 tetrahedra: two in $<110>$ direction (first layer) and two $<1-10>$ direction (second layer), this is the diamond unit cell with missing four neighboring tetrahedral; and (f) Diamond unit cell with missing four atoms from neighboring tetrahedra.

both involve the random arrangement of tetrahedra, however, the number density of these tetrahedra in Q-silicon is considerably higher than in ion-implanted amorphous silicon. In ion-implanted silicon, there is 100% sp^3 bonding and dangling bonds between the tetrahedra are saturated with no unpaired spins. We discuss the details of the atomic structure of Q-silicon phases and the phenomenon of polyamorphism related to distinct amorphous phases of Q-silicon. The unpaired spins in amorphous Q-silicon, consisting of randomly packed tetrahedra, can have dangling bonds and unpaired spins between the tetrahedra, where these spins provide the source for bulk paramagnetism and ordered ferromagnetism, as shown for Q-carbon [2–5]. It should be mentioned that dopants such as boron can eliminate unpaired spins and the ferromagnetism associated with them, and lead to high-temperature superconductivity, as elegantly demonstrated in highly B-doped Q-carbon [8–12].

Results and discussion

Atomic structure and design of amorphous Q-phases

The basic building block in both amorphous and crystalline Q-phases is silicon/diamond cubic tetrahedron, as shown in Figure 1(a). This tetrahedron (D1) is contained in $a/2, a/2, a/2$ or one-eighth of the diamond cubic unit cell. The tetrahedron consists of two triangular units, which are arranged in perpendicular $<110>$

and $<1-10>$ directions. These triangular units, which are bonded in $<111>$ directions, represent the basic characteristics of covalent bonding. These tetrahedra can grow along $<110>$ directions into two (D2), as shown in Figure 1(b). Figure 1(c) shows three tetrahedra (D3) along $<110>$ direction. It should be noted that these tetrahedra are joined along $<001>$ axis, around which they can pivot and form a long ring or a string structure. These ring and string structures can play a critical role in enhancing the mobility of carriers. If the third tetrahedron joins along $<1-10>$ instead of $<110>$ in the second plane, we form D3+, as shown in Figure 1(d). It is interesting to note that D3+ is a precursor to the diamond cubic unit cell. When the fourth tetrahedron joins along $<1-10>$ direction in the second plane, it becomes a silicon/diamond cubic unit cell, as shown in Figure 1(e). Here, all the atoms are tetrahedrally bonded by four atoms, which leaves a net of eight atoms in the unit cell. The silicon cubic unit cell, as shown in Figure 1(f), has four corner atoms, which are shared by four atoms with a net of one atom. If the corner atoms are shared by eight unit cells, we also have a net one atom. With these building blocks (D1, D2, D3, and D3+), we can create new phases, named Q-phases of silicon, which are in parallel to distinct Q-phases of carbon and BN, namely, Q1, Q2, and Q3. These Q-phases are expected in all the materials of zinc blende structures with a higher number density of atoms than diamond cubic unit cell and exhibit novel properties [4,5,8,9].

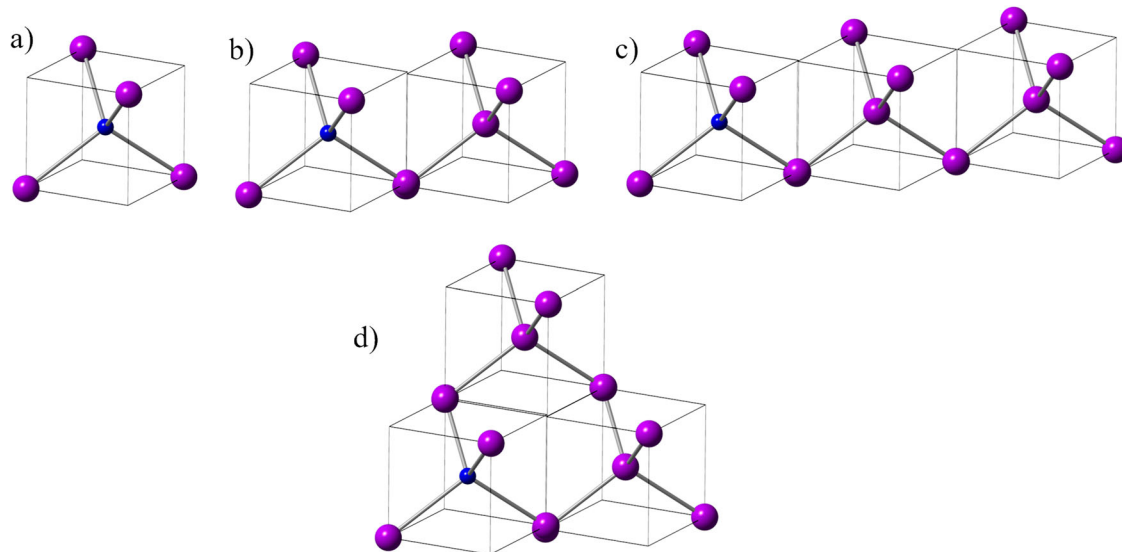


Figure 2. (a) Formation of QB3, when one central C atom is replaced by B in a three-unit (trimer) tetrahedra; (b) Formation of QB2, when one central C atom is replaced by B in a two-unit (dimer) tetrahedral; (c) Formation of QB1, when one central C atom is replaced by B in a three-unit tetrahedra (trimer); and (d) Formation of QB1, when one central C atom is replaced by B in a three-unit tetrahedra in two layers.

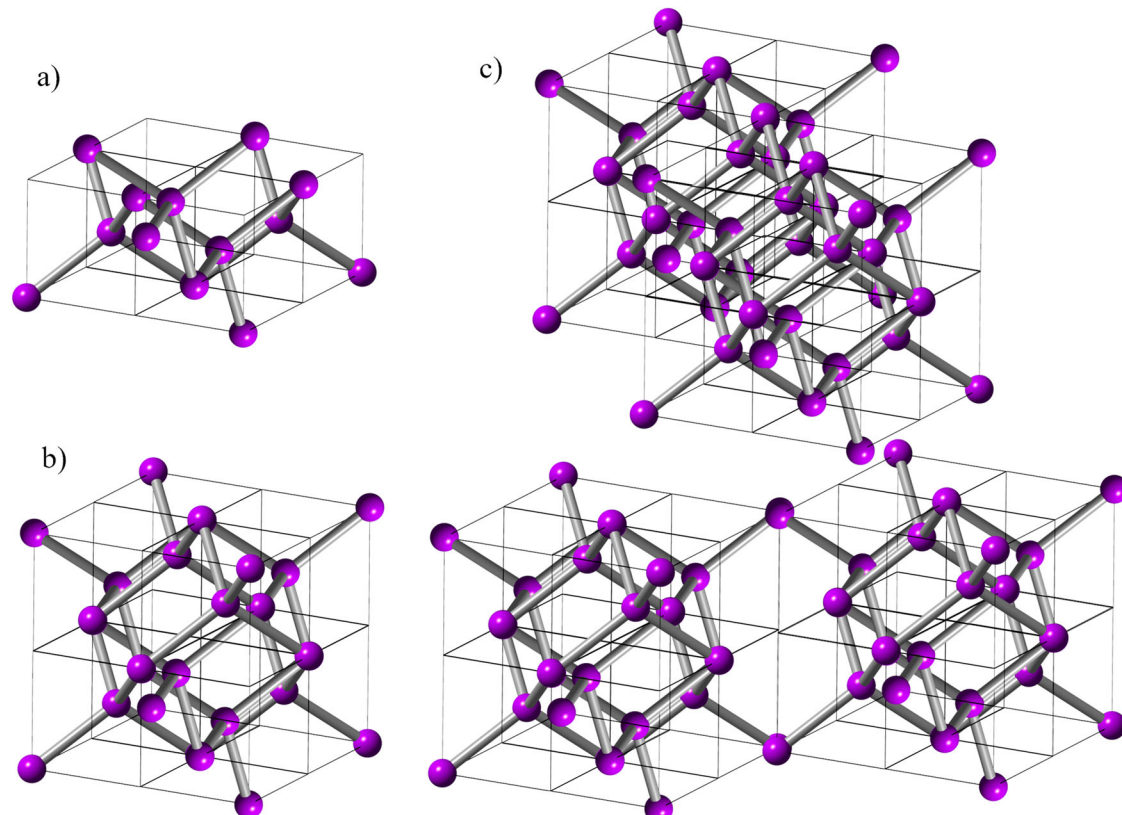


Figure 3. (a) Four D1 tetrahedra in one plane (D14); (b) Eight tetrahedra in two planes, leading to formation of Q-diamond subunit cell with net 16 atoms; and (c) Formation of Q-diamond super unit cell with four subunit cells: two in $\langle 110 \rangle$ direction and two in $\langle 1-10 \rangle$ direction (d) with missing four neighboring subunit cells, similar to missing tetrahedra in the diamond unit cell. By replacing central C atoms in these tetrahedra by B atoms selectively, 50% B-doped Q-diamond phase is created, having net 32 C and 32 B atoms arranged in two layers.

Formation and doping of amorphous Q-silicon

When D1, D2, and D3 and D3+ tetrahedral units are packed randomly, we create Q3, Q2, and Q1 phases of Q-silicon. It has been shown through geometrical and theoretical modeling that tetrahedral units can be packed randomly with a packing efficiency of $\geq 80\%$ [13]. However, the packing of diamond tetrahedra with covalent dangling bonds at the surfaces may pose additional constraints. These distinct phases represent three allotropes of Q-silicon and the phenomenon of polymorphism in silicon. By replacing one silicon with boron, for example, the central atom in the tetrahedron, we can create B-doped Q-silicon with dopant concentrations far exceeding the thermodynamic solubility limit. By replacing the central atom in the D1 tetrahedron with boron (Figure 2(a)) and packing randomly, we create 50at% B-doped Q-silicon (QB3 silicon). By replacing the central atom with boron in one of the two tetrahedra in D2 (dimer as shown in Figure 2(b)) and packing randomly, we create 25at% B-doped Q-silicon (QB2 silicon). Similarly, by replacing the central atom with boron in one of the three tetrahedra in D3 (trimer as shown in Figure 2(c)) and packing randomly, we create 17at% B-doped Q-silicon (QB1 silicon). The QB1 is also formed, when one central C atom is replaced by B in a three-unit tetrahedra in two layers (as shown in Figure 2(d)). These allotropes of silicon may have different electrical, optical, and mechanical properties, as demonstrated by robust ferromagnetism in undoped Q-carbon and record BCS superconducting properties of B-doped Q-carbon, where QB1, QB2, and QB3 showed T_c of 37, 57 K, and > 250 K, respectively [8–12]. We also anticipate that there may be issues related to lattice strain. As boron enters substitutional sites in the diamond crystalline lattice it could generate unwanted tensile strain (covalent radius of B = 0.082 nm; and covalent radius of silicon = 0.117 nm), which could lead to disorder scattering and breaking up of the Cooper pairs. It should be noted that the issue related to dopant misfit strains in amorphous structures will be considerably less than crystalline counterparts.

Formation and doping of crystalline Q-silicon

When four D1 tetrahedra get together in one plane, we create the basic unit cell (D14) for the formation of crystalline Q-silicon, as shown in Figure 3(a). By adding another fourth tetrahedra in the second plane, we create Q-silicon subunit cell, as shown in Figure 3(b). These subunit cells can grow only along $<110>$ direction, as the face atoms are already saturated with four covalent bonds. When the third subunit cell joins in $<1-10>$ direction in the second plane, we have created a precursor

to a crystalline Q-silicon super unit cell. This super unit cell for crystalline Q-silicon is completed by putting the fourth subunit cell in $<1-10>$ direction in the second plane. It should be noted that the super unit cell contains net 64 atoms with a lattice constant of 1.086 nm. Thus, while the number density of the sub unit cell locally is $16/a^3$, the average number density for the super unit cell is $8a^3$, which is the same as the cubic diamond unit cell. Thus, by replacing the tetrahedra with the subunit cell with both having a number density of $16/a^3$, we achieve Q-silicon structure. This is a very interesting parallel between a diamond cubic lattice and Q-silicon lattice, where local structures having double the number density of atoms alternate with empty spaces for a net half the number density of atoms.

Table 1 shows the coordinates of atoms in all four subunits (A1, A2, B1, and B2) of a super unit cell. There are 22 atoms (8 corners + 6 faces + 8 inside) in each subunit with one common (C^*) to all, and the other three atoms between two subunits, leaving 79 distinct atomic positions. In Table 1, rows of atoms 1 through 14 represent corner and face atoms, and rows 15 through 22 are 8 inside atoms. For doping purposes, the rows of inside atoms can be replaced by dopants with each row accounting for 6.25 at%. The replacement of two rows 15 and 16 leads to 12.5 at% B-doped Q-silicon. For the boron doping of silicon, this is far higher than the thermodynamic solubility limit of 1.2 at% of B in silicon. To achieve these higher dopant concentrations we need to adopt highly nonequilibrium methods to trap kinetically the dopants in higher energy states by nanosecond laser melting and quenching. More recently, we have shown that low-energy ion implantation of amorphous carbon can lead to Q-carbon conversion over a large area with a wafer-scale integration [14].

Experimental details

The Si (100) and Si (111) substrates ~ 400 μm thick were irradiated with 100 keV Ge $^+$ and As $^+$ ions to a dose of 1.0×10^{16} ions. cm^{-2} . The Ge $^+$ and As $^+$ ions of similar mass produce high enough nuclear-stopping damage to amorphize crystalline silicon to a depth of about 170 nm, with Ge $^+$ ions creating undoped amorphous layers. The ions are implanted beyond the critical angle of channeling of about 3 degrees. We have calculated the range analytically which matched with TRIM calculations. Pulsed laser annealing was carried out using ArF excimer laser (193 nm wavelength, and 20 ns pulse duration, capacitor/pumping voltage = 21 KV, gas pressure = 3200 mbar, and dimension of beam spot = 10×5 mm 2) with a single pulse of energy density varied between 0.1 and 0.3 J/cm $^{-2}$.

Table 1. Atom coordinates for B-doped Q-carbon subunit cell and super unit cell. Four common atomic positions between different subunit cells are indicated by C* and common between A and B subunits.

B1	A2	A1	A2	B1	B2
A1	B2	$a = 0.71\text{nm}$	$a/2[110]$	$a/2[011]$	$a/2[101]$
	atoms	A1	A2	B1	B2
C	1	0, 0, 0	1/2, 1/2, 0	A2A1	0, 1/2, 1/2
	2	1/2, 0, 0	1, 1/2, 0		1/2, 0, 1/2
	3	1/2, 1/2, 0	A1A2	1/2, 1, 1/2	C*
	4	0, 1/2, 0	1, 1, 0	B1A1	1, 0, 1/2
	5	1/4, 0, 1/4	1/2, 1, 0	B1A2	1, 1/2, 1/2
	6	1/2, 1/4, 1/4	3/4, 1/2, 1/4		B2A1
	7	1/4, 1/2, 1/4	1/2, 3/4, 1/4	1/4, 1/2, 3/4	C*
	8	0, 1/4, 1/4	1/2, 1/4, 1/4	1/2, 1/4, 1/2	3/4, 0, 3/4
	9	1/4, 1/4, 0	3/4, 3/4, 0	1/2, 3/4, 3/4	1, 1/4, 3/4
	10	1/4, 1/4, 1/2	3/4, 3/4, 1/2	1/4, 1, 3/4	3/4, 1/2, 3/4
	11	0, 0, 1/2	1/2, 1/2, 1/2	0, 3/4, 3/4	1/2, 1/4, 3/4
	12	1/2, 0, 1/2	A1B2	1/4, 3/4, 1/2	3/4, 1/4, 1/2
	13	1/2, 1/2, 1/2	C*	1/4, 3/4, 1	3/4, 1/4, 1
B	14	0, 1/2, 1/2	A1B1	0, 1/2, 1	1/2, 0, 1
	15	1/8, 1/8, 1/8	1/2, 1/2, 1/2	1/2, 1/2, 1	1, 0, 1
	16	3/8, 3/8, 3/8	A2B2	1/2, 1/2, 1	1/2, 1/2, 1
	17	3/8, 1/8, 1/8	A2B1	0, 1, 1	1/2, 1/2, 1
	18	1/8, 3/8, 3/8			B2B1
	19	3/8, 3/8, 1/8			
	20	1/8, 1/8, 3/8			
	21	1/8, 3/8, 1/8			
	22	3/8, 1/8, 3/8			

Microstructure and atomic structure determinations of Q-silicon were carried out by using high-resolution scanning electron microscopy (HRSEM), electron backscatter diffraction (EBSD), and (scanning) transmission electron microscopy (STEM and TEM). The bonding characteristics were determined by core-loss EELS and Raman spectroscopy. We performed HRSEM studies using secondary and back-scattered electrons (having a sub-nanometer resolution) in an FEI Verios 460L SEM. The TEM/STEM cross-section samples are prepared by FIB milling using ThermoFisher Quanta 3D FEG microscope. The aberration-corrected STEM-ThermoFisher Titan 80-300 was used to perform the (scanning) transmission electron microscopy. The EELS scans were performed by using the EELS detector mounted in the STEM-ThermoFisher Titan 80-300 microscope. The Raman measurements were made using the Alfa300 R superior confocal Raman spectrometer (lateral resolution $< 200\text{ nm}$) having 532 nm excitation source. The Raman spectrometer was calibrated by using a standard crystalline Si sample with a vibrational mode (Raman peak) at 520.6 cm^{-1} . Magnetic measurements were performed in magnetic fields up to 1 T in an Ever-Cool Quantum Design PPMS system with a base temperature as low as 10 K.

Experimental results

By nanosecond laser melting of amorphous silicon and rapid quenching from the highly undercooled state, we can create amorphous and crystalline Q-silicon [15,16].

The molten silicon is metallic, where electrons are delocalized and atoms are closely packed. In the under-cooled state, electrons start to delocalize and form diamond tetrahedra with covalent bonds. Depending upon the time available in the undercooled state, we form amorphous Q-silicon, crystalline Q-silicon, or zinc blende silicon with increasing time. The cross-section TEM micrograph in Figure 4 (a) shows clearly the formation of Q-silicon band $85 \pm 5\text{ nm}$ wide for 0.3 Jcm^{-2} sample, which is followed by an amorphous silicon layer of $85 \pm 5\text{ nm}$ wide created by Ge^+ ion implantation. The selected-area diffraction pattern (shown in the inset) shows (111) and (200) diffraction rings, in addition to diffused rings from amorphous zinc blende and Q-silicon. The crystalline Q-silicon shows (200) diffraction spots (inset), which are missing in normal cubic zinc blende structure, as shown by structure factor calculations of Q-phases. The new Q-phase structure has 3 Si atoms (Si_0 (0,0,0), Si_1 (1/4,1/4,1/4), and Si_2 (1/4,1/4,3.4)) forming the basis for the FCC lattice instead of two Si atoms in Diamond Cubic phase (Si_0 and Si_1 only). The structure factor of DC-Si is

$$F_{DC-Si} = f_{Si} \left[1 + e^{\frac{\pi(h+k+l)}{2}} \right] \left[1 + e^{\frac{\pi(h+k)}{2}} + e^{\frac{\pi(k+l)}{2}} + e^{\frac{\pi(h+k)}{2}} \right] \text{ whereas structure of Q-Si is } F_{Q-Si} = f_{Si} \left[1 + e^{\frac{\pi(h+k+l)}{2}} + e^{\frac{\pi(h+k+3l)}{2}} \right] \left[1 + e^{\frac{\pi(h+k)}{2}} + e^{\frac{\pi(k+l)}{2}} + e^{\frac{\pi(h+k)}{2}} \right].$$

For a $[01\bar{1}]$ zone axis, it allows presence of (200) planes [$|F_{Q-Si}|^2 = 16f_{Si}^2$], which was not possible in diamond cubic structures ($|F_{DC-Si}|^2 = 0$). Figure 4(c) shows a high-resolution TEM of an interface between Q-silicon

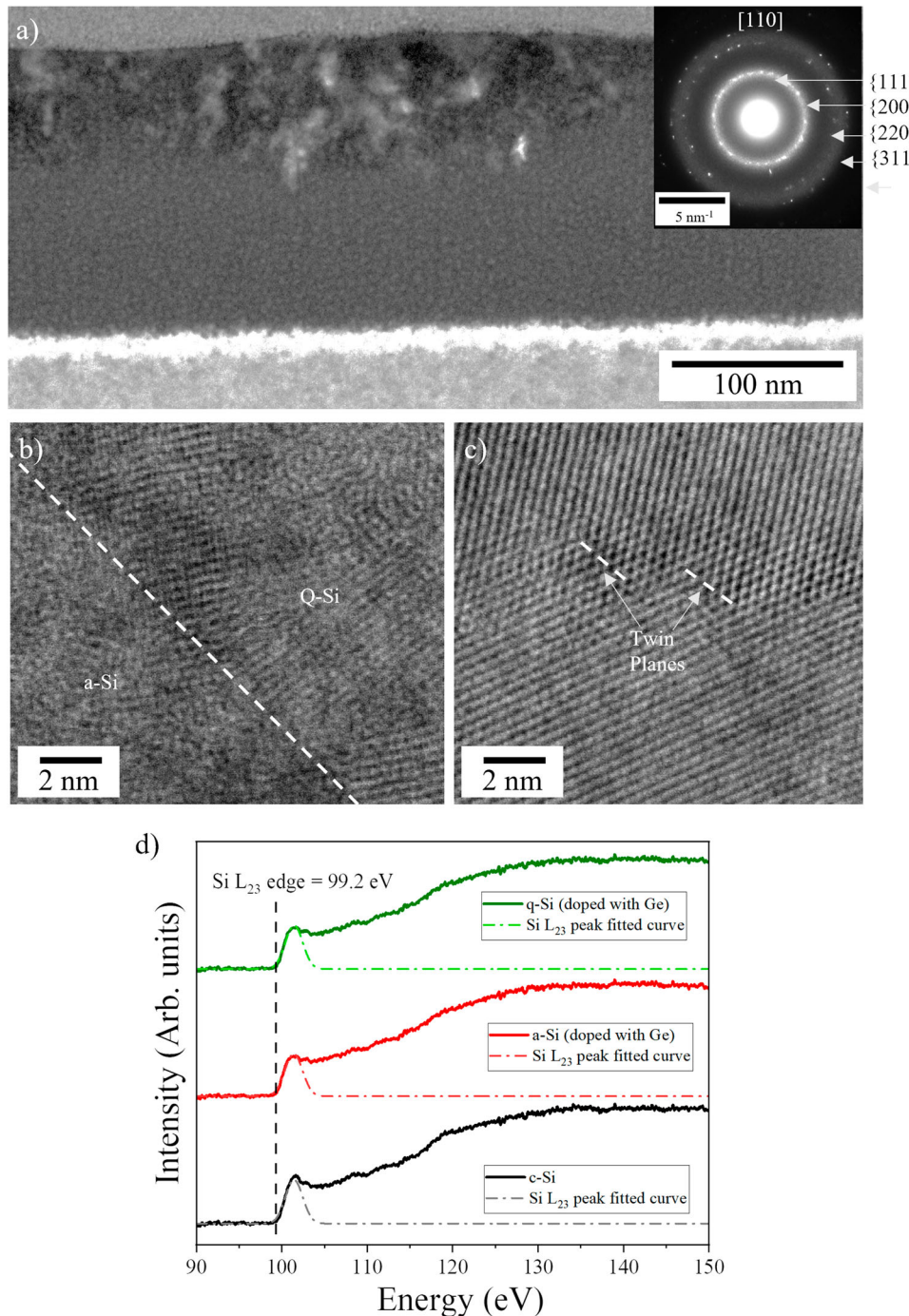


Figure 4. High-resolution TEM micrograph showing formation of Q-silicon: (a) $<110>$ cross-section TEM with 85 ± 5 nm Q-silicon layer and inset diffraction pattern with 111, 200, 220, and 311 continuous diffraction rings; (b) Interface between Q-silicon and amorphous silicon; and (c) Nanocrystallites in Q-silicon with nanotwins. (d) EELS spectrum from crystalline (c-Si), amorphous (a-Si) and Q-silicon (Q-Si), showing Si L₂₃ edge remains unchanged

and amorphous silicon. The amorphous Q-silicon contains nanocrystallites of zinc blende silicon (Figure 4(b)). It is interesting to note that some of the nanocrystallites contain nanotwins as a result of rapid quenching, as shown in Figure 4(c). Figure 4(d) shows EELS spectra from crystalline silicon, Ge⁺ ion-implanted amorphous silicon, and Q-silicon. The Si L_{2,3} edge structures

at 99.2 eV in all three cases remain the same, indicating 100% sp³ bonding in all three cases.

Figure 5 shows results from Raman spectroscopy of amorphous silicon before laser annealing (Figure 5(a)) and after laser annealing with 0.1, 0.2, and 0.3 Jcm⁻² in Figures 5(b, c and d), respectively. The Raman spectra contain TA (transverse acoustic), LA (longitudinal

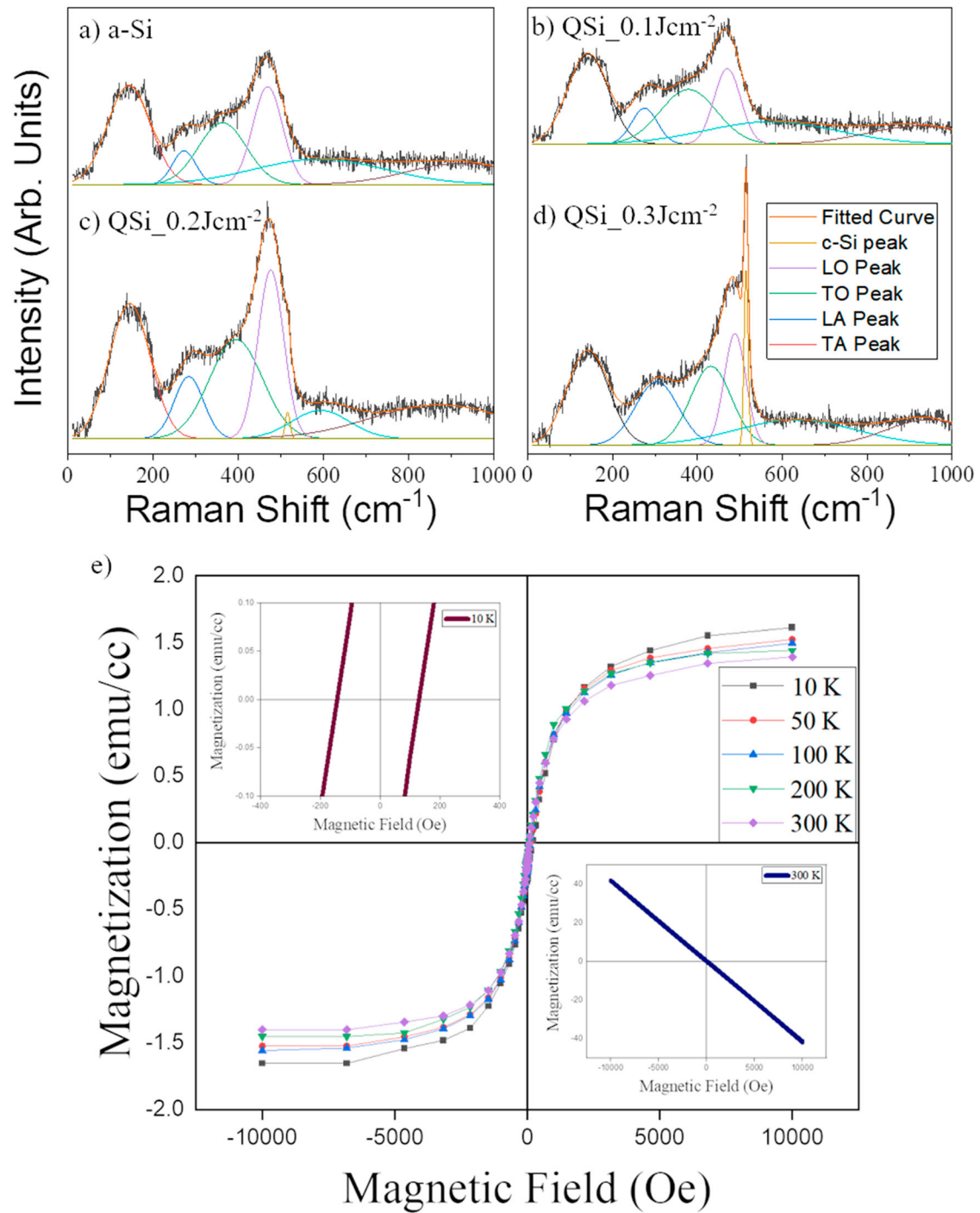


Figure 5. Raman Spectra: (a) Unannealed amorphous silicon (Ge^+ implanted); (b) Laser annealed with 0.1 Jcm^{-2} (c) Laser annealed with 0.2 Jcm^{-2} , (d) Laser annealed with 0.3 Jcm^{-2} , and (e) Magnetization (M) versus field (H) at 10 K , 50 K , 100 K , 200 K and 300 K of 0.3 Jcm^{-2} sample with inset (top left) showing coercivity associated with ferromagnetism (intercept along the x-axis), and other inset (bottom right) showing diamagnetic behavior in as-implanted samples before laser annealing.

acoustic), LO (longitudinal optic), and TO (transverse optic) modes. Table 2 shows a detailed analysis of the variation of these modes and crystalline Si peaks as a function of laser pulse energy density. As the pulse energy density increases TO mode frequency increases, which is indicative of increasing bond energy in laser annealed

Q-silicon. The structure of Q-silicon after annealing with 0.1 Jcm^{-2} pulse is totally amorphous, however, the crystalline fraction appears after 0.2 Jcm^{-2} and increases at 0.3 Jcm^{-2} . This is indicative of the fact that as the energy density increases, melt lifetime increases and more time is available for crystal growth. These results are consistent

Table 2. TA, LA, LO, TO and crystalline modes in Raman spectra of Figure 5, before annealing and after annealing with 0.1, 0.2, and 0.3 Jcm⁻².

	TA		LA		LO		TO		Crystalline	
	Peak	%	Peak	%	Peak	%	Peak	%	Peak	%
Unannealed	142.76	39	272.49	7.2	362.36	27.2	468.69	26.6	—	—
0.1Jcm ⁻²	141.79	38.08	275.43	9.54	378.83	31.7	470.38	20.69	—	—
0.2Jcm ⁻³	144.81	32.43	283.6	10.64	394.58	30.84	476.05	25.34	515.57	0.75
0.3Jcm ⁻³	141.66	30.24	304.17	21.01	431.83	24.73	488.38	18.53	514.49	5.44

with detailed cross-section TEM results. The crystalline silicon nucleates from the undercooled molten silicon and size of nanocrystallites depends upon the time available for crystal growth. It is interesting to note that nanocrystalline peaks are downshifted from 520.6 cm⁻¹ to 515 cm⁻¹ due to quantum confinement effects.

Figure 5(e) shows that ion-implanted (100 KeV Ge⁺ with a dose = 1.0×10^{16} cm⁻²) is diamagnetic, as indicated in the inset. Interestingly, M vs H plot shows a robust ferromagnetic behavior at 10 K, 50 K, 100 K, 200 K, and 300 K. From saturation magnetization as a function, we estimated Curie temperature above 600 K using the Block formula. The blocking temperature from M vs T plots (Figure S1) has been estimated to be greater than 400 K. These measurements were carried out for the sample annealed at 0.3 Jcm⁻² (ArF Excimer laser with 193 nm wavelength, and pulse duration 20 ns). The laser-annealed silicon exhibits finite coercivity of 100 Oe (intercept along the x-axis in the top left inset), which is characteristic of long-range ferromagnetic ordering. It should be noted that amorphous silicon before laser annealing shows a diamagnetic behavior (bottom right inset), where silicon dangling bonds between tetrahedra are saturated. The tetrahedra in as-implanted amorphous silicon are not as closely packed as in Q-silicon, and sp³ dangling bonds find their way to reconstruct. On the other hand, in amorphous Q-silicon, the tetrahedra are closely packed, leaving dangling bonds between them. In addition, the dangling bonds at the interface between the amorphous and nanocrystalline regions can lead to dangling bonds.

Conclusions

We have presented atomic structures of amorphous and crystalline Q-silicon, which can be doped with concentrations far exceeding the thermodynamic solubility limits through the solute trapping phenomenon. The basic unit of Q-phases is a diamond tetrahedron with an atomic number density of 16/a³. By packing them randomly with the units of one, two, and three tetrahedra, we create distinct phases Q3, Q2, and Q1 of silicon, which have much higher number density (> 60%) of atoms than that of cubic zinc blende structure. The cubic zinc blende

structure of silicon is formed by putting two tetrahedra in <110> direction followed by two in <1-10> in the next plane. This leaves alternate empty spaces and explains the lower density of atoms 8/a³ in cubic zinc blende structure with an atomic packing fraction of only 34%. Thus, three tetrahedra in two adjacent planes are a precursor to the cubic unit cell. By putting together eight tetrahedral without empty spaces, we create sub unit cell for crystalline Q-silicon with sixteen atoms, having eight inside, six face atoms, and eight corner atoms. This is similar to the calcium fluoride structure. However, in this case with covalent bonding, face atoms are already coordinated with four atoms. As a result, to form a three-dimensional crystalline structure, these sub unit cells are arranged two in <110> and two in <1-10> directions to form a super unit cell of sixty atoms, as shown in Table 1. This arrangement leaves alternate empty spaces, similar to the tetrahedral arrangement in the diamond cubic lattice. It is interesting to note that while sub unit cells have number density of atoms of 16/a³, the super unit cell has only 8/a³. By replacing Si atoms with dopants, Q-phases can be doped with distinct concentrations far higher than thermodynamic dopant solubility limits. The Q-phases can accommodate dopant size misfit-induced strains more effectively and lead to less carrier scattering.

It is found that amorphous Q-silicon can have dangling bonds and unpaired spins between the tetrahedra, which provide the source for bulk paramagnetism and ordered ferromagnetism. Dangling bonds in covalently silicon-based materials can provide a source for paramagnetism and ordered ferromagnetism. Nevertheless, the dangling bonds in the bulk of these materials reconstruct to eliminate sources for paramagnetism and ferromagnetism. However, unreconstructed dangling bonds on surfaces, steps, and kinks can provide sources of electron spins with atomic-scale paramagnetism and ferromagnetism. Discovery of Q-silicon stands to revolutionize modern microelectronics by adding new functionalities, such as spintronics on a chip. Modern microelectronics is based upon the charge of an electron, making them slow with limited mobility. By using the Q-silicon, we make use of the spin of the electron, making computer much faster with negligible power consumption [17].

We have also shown B-doped Q-silicon phases to be superconducting as a result of a higher number density of states near the Fermi level, and an optimum combination of phonon hardening within tetrahedra and phonon softening because of alternate empty spaces. Theoretical results for 12.5at% B-doped crystalline Q-silicon show frequency (RMS) average as $\omega_{ph} = 300$ - 400 cm^{-1} , and cut-off frequency $\Omega = 1000\text{ cm}^{-1}$. From these values, the superconducting transition temperature (T_c) is estimated as $T_c = 174\text{ K}$, 171 K , and 167 K for $\omega_{ph} = 300\text{ cm}^{-1}$, 350 cm^{-1} , and 400 cm^{-1} , respectively [18].

Acknowledgements

This work was supported in part by the National Science Foundation (Grants 1836767 and 2029974). We also acknowledge the contributions of Dr. Chris Winkler for TEM/STEM studies, and Minghao Pan for theoretical calculations, the details of which will be reported shortly.

Disclosure statement

No potential conflict of interest was reported by the authors.

Funding

This work was supported by National Science Foundation: [Grant Number 1836767,2029974].

References

- [1] Erwin SC, Himpel FJ. Intrinsic magnetism at silicon surfaces. *Nat Commun.* **2010**;1:58. doi:[10.1038/ncomms1056](https://doi.org/10.1038/ncomms1056)
- [2] Narayan J, Bhaumik A. Novel phase of carbon, ferromagnetism, and conversion into diamond. *J Appl Phys.* **2015**;118:215303. doi:[10.1063/1.4936595](https://doi.org/10.1063/1.4936595)
- [3] Sachan R, Hatchtel J, Bhaumik A, et al. Emergence of shallow energy levels in B-doped Q-carbon: a high-temperature superconductor. *Acta Mater.* **2019**;174: 153–159. doi:[10.1016/j.actamat.2019.05.013](https://doi.org/10.1016/j.actamat.2019.05.013)
- [4] Bhaumik A, Sachan R, Narayan J. Magnetic relaxation and three-dimensional critical fluctuations in B-doped Q-carbon – a high-temperature superconductor. *Nanoscale.* **2018**;10:12665–12673. doi:[10.1039/C8NR03406K](https://doi.org/10.1039/C8NR03406K)
- [5] Bhaumik A, Nori S, Sachan R, et al. Room-Temp ferromagnetism and extraordinary Hall effect in nanostructured Q-carbon: implications for potential spintronic devices. *ACS Appl. Nano Mater.* **2018**;1:807–819. doi:[10.1021/acsanm.7b00253](https://doi.org/10.1021/acsanm.7b00253)
- [6] Mal S, Nori S, Jin C, et al. Reversible room temperature ferromagnetism in undoped zinc oxide: correlation between defects and physical properties. *J Appl Phys.* **2010**;108(7):073510. doi:[10.1063/1.3491037](https://doi.org/10.1063/1.3491037)
- [7] Wang YF, Shao YC, Hsieh SH, et al. Origin of magnetic properties in carbon implanted ZnO nanowires. *Sci Rep.* **2018**;8(1):7758. doi:[10.1038/s41598-018-25948-x](https://doi.org/10.1038/s41598-018-25948-x)
- [8] Narayan J, Bhaumik A, Sachan R. High temperature superconductivity in distinct phases of amorphous B-doped Q-carbon. *J Appl Phys.* **2018**;123:135304. doi:[10.1063/1.5016397](https://doi.org/10.1063/1.5016397)
- [9] Narayan J, Sachan R, Bhaumik A. Search for near room-temperature superconductivity in B-doped Q-carbon. *Mater. Res. Lett.* **2019**;7:164–172. US Patents: 10586702 and 10566193. doi:[10.1080/21663831.2019.1569566](https://doi.org/10.1080/21663831.2019.1569566)
- [10] Bhaumik A, Sachan R, Gupta S, et al. Discovery of high-temperature superconductivity ($T_c = 55\text{ K}$) in B-doped Q-carbon. *ACS Nano.* **2017**;11:11915–11922. doi:[10.1021/acsnano.7b06888](https://doi.org/10.1021/acsnano.7b06888)
- [11] Bhaumik A, Narayan J. Structure–property correlations in phase-pure B-doped Q-carbon high-temperature superconductor with a record $T_c = 55\text{ K}$. *Nanoscale.* **2019**;11:9141–91543. doi:[10.1039/C9NR00562E](https://doi.org/10.1039/C9NR00562E)
- [12] Sakai Y, Chelikowsky JR, Cohen ML. Simulating the effect of boron doping in superconducting carbon. *Phys Rev B.* **2018**;97:054501. doi:[10.1103/PhysRevB.97.054501](https://doi.org/10.1103/PhysRevB.97.054501)
- [13] Jaoshvili A, Esakia A, Porrati M, et al. Experiments on the random packing of tetrahedral dice. *Phys Rev Lett.* **2010**;104:185501. doi:[10.1103/PhysRevLett.104.185501](https://doi.org/10.1103/PhysRevLett.104.185501)
- [14] Narayan J, Bhaumik A, Gupta S, et al. Laser processing of continuous and adherent diamond films on sapphire and glass. *Carbon N Y.* **2021**;176:558–568. doi:[10.1016/j.carbon.2021.02.049](https://doi.org/10.1016/j.carbon.2021.02.049)
- [15] Singh RK, Narayan J. Mater Sci Eng. **1989**;B3:217–230. doi:[10.1016/0921-5107\(89\)90014-7](https://doi.org/10.1016/0921-5107(89)90014-7)
- [16] Lowndes DH, Wood RF, Narayan J. *Phys Rev Lett.* **1984**;52:561–564. doi:[10.1103/PhysRevLett.52.561](https://doi.org/10.1103/PhysRevLett.52.561)
- [17] Narayan J, Narayan RJ. US Patent Serial No.: 63/461,015; Filing Date: April 21, 2023.
- [18] Pan M, Kim KW, Narayan J. to be Published.